

STAR FORMATION AT $Z \sim 6$: THE UDF-PARALLEL ACS FIELDS¹

R.J. BOUWENS², G.D. ILLINGWORTH², R.I. THOMPSON³, J.P. BLAKESLEE⁴, M.E. DICKINSON⁵, T.J. BROADHURST⁶, D.J. EISENSTEIN³, X. FAN³, M. FRANX⁷, G. MEURER⁴, P. VAN DOKKUM⁸

1 Based on observations made with the NASA/ESA Hubble Space Telescope, which is operated by the Association of Universities for Research in Astronomy, Inc., under NASA contract NAS 5-26555. These observations are associated with programs #9803.

2 Astronomy Department, University of California, Santa Cruz, CA 95064

3 Steward Observatory, University of Arizona, Tucson, AZ 85721.

4 Department of Physics and Astronomy, Johns Hopkins University, Baltimore, MD 21218.

5 National Optical Astronomy Obs., P.O. Box 26732, Tucson, AZ 85726.

6 Racah Institute of Physics, The Hebrew University, Jerusalem, Israel 91904.

7 Leiden Observatory, Postbus 9513, 2300 RA Leiden, Netherlands.

8 Department of Astronomy, Yale University, New Haven, CT 06520.

Draft version October 29, 2019

ABSTRACT

We report on the i -dropouts detected in two exceptionally deep ACS fields (B_{435} , V_{606} , i_{775} , and z_{850} with 10σ limits of 28.8, 29.0, 28.5, and 27.8, respectively) taken in parallel with the UDF NICMOS observations. Using an $i - z > 1.4$ cut, we find 30 i -dropouts over 21 arcmin² down to $z_{850,AB} = 28.1$, or 1.4 i -dropouts arcmin⁻², with significant field-to-field variation (as expected from cosmic variance). This extends i -dropout searches some $\sim 0.9^m$ further down the luminosity function than was possible in the GOODS field, netting a $\sim 7\times$ increase in surface density. An estimate of the size evolution for UV bright objects is obtained by comparing the composite radial flux profile of the bright i -dropouts ($z_{850,AB} < 27.2$) with scaled versions of the HDF-N + HDF-S U -dropouts. The best-fit is found with a $(1+z)^{-1.57^{+0.50}_{-0.53}}$ scaling in size (for fixed luminosity), extending lower redshift ($1 < z < 5$) trends to $z \sim 6$. Adopting this scaling and the brighter i -dropouts from both GOODS fields, we make incompleteness estimates and construct a $z \sim 6$ LF in the rest-frame continuum UV ($\sim 1350\text{\AA}$) over a 3.5 magnitude baseline, finding a shape consistent with that found at lower redshift. To evaluate the evolution in the LF from $z \sim 3.8$, we make comparisons against different scalings of a lower redshift B -dropout sample. Though a strong degeneracy is found between luminosity and density evolution, our best-fit model scales as $(1+z)^{-2.8}$ in number and $(1+z)^{0.1}$ in luminosity, suggesting a rest-frame continuum UV luminosity density at $z \sim 6$ which is just $0.38^{+0.09}_{-0.07} \times$ that at $z \sim 3.8$. Our inclusion of size evolution makes the present estimate lower than previous $z \sim 6$ estimates.

Subject headings: galaxies: evolution — galaxies: high-redshift — galaxies: luminosity function, mass function

1. INTRODUCTION

The unique deep z -band capabilities of the Hubble Space Telescope (HST) Advanced Camera for Surveys have uncovered a substantial population of $z \sim 6$ dropouts (e.g., Yan, Windhorst, & Cohen 2003). Early estimates indicate that the star formation rate at $z \sim 6$ is only somewhat lower than (only 0.17-0.77 \times that) at $z \sim 3$ (Bouwens et al. 2003b; Stanway, Bunker, & McMahon 2003; Dickinson et al. 2004; Stanway et al. 2004; Bouwens et al. 2004, hereinafter, B04). Unfortunately, these early studies have all been on fields of somewhat intermediate depth, with strong incompleteness corrections beyond $z_{850,AB} = 26.5$. Since a simple extrapolation of the Steidel et al. (1999) $z \sim 3$ luminosity function to $z \sim 6$ predicts an L_* of $z_{850,AB} = 26$, these samples are becoming incomplete just as the i -dropouts are starting to become prominent. Moreover, the substantial biases against larger, lower surface brightness objects make it difficult to derive the size distribution at $z \sim 6$ (e.g., B04 find that only $\sim 25\%$ of the brighter U -dropouts make it into their $z \sim 6$ Great Observatories Origins Deep Survey (GOODS) sample). It is therefore important to examine i -dropouts in a much deeper field.

Here we report on observations of i -dropouts from two exceptionally deep ACS Wide Field Camera (WFC) parallels (hereinafter, UDF-Ps) that were taken in conjunction with Near Infrared Camera and Multi-Object Spectrometer (NICMOS) observations of the Ultra Deep Field (UDF) (GO-9803; Thompson et al. 2004). 9, 9, 18, and 27 orbits were taken in the F435W, F606W, F775W, and F850LP passbands (hereinafter called B_{435} , V_{606} , i_{775} , and z_{850}) for each field over 9 pointings (the pointings were arranged in a 3×3 grid, each separated by 45"). These observations extend i -dropout searches some 0.9^m magnitude deeper than GOODS and to within 0.9^m magnitudes of the UDF, giving a preview of the results at these depths. We assume $(\Omega_M, \Omega_\Lambda, h) = (0.3, 0.7, 0.7)$ (Bennett et al. 2003).

2. OBSERVATIONS

These observations were retrieved from STScI and subject to the standard CALACS on-the-fly reprocessing (OTFR). Additional processing, including cosmic-ray rejection, alignment, and final image combination, was performed by the "Apsis" data reduction software (Blakeslee et al. 2003). The latest photometric zero points were applied (Sirianni et al. 2004) along with a correction for galactic absorption (Schlegel, Finkbeiner, & Davis 1998). The 10σ limiting

magnitudes (for the deepest parts of the image) were approximately 28.8, 29.0, 28.5, and 27.8 in the B_{435} , V_{606} , i_{775} , and z_{850} bands, respectively, with PSF FWHMs of 0.08-0.09''.

3. ANALYSIS

Areas whose V , i , and z exposures were shorter than 5, 10, and 15 orbits were excluded from the analysis. Object detection and photometry was performed on the remaining area for each parallel (21 arcmin 2 , in total) using SExtractor (Bertin & Arnouts 1996) with smaller scaled apertures (MAG_AUTO) to measure colors and larger scaled apertures to correct to total flux. For our i -dropout selection, we apply a similar i -dropout selection criteria to that used by B04 on the GOODS data set. We require objects be a 5.5 σ -detection within a 0.25''-diameter aperture, have a SExtractor stellarity less than 0.85 (non-stellar to high confidence), have $(i_{775} - z_{850})_{AB}$ colors redder than 1.4, and be a non-detection ($< 2\sigma$) in the V_{606} band (within the smaller-scaled apertures). Several studies have demonstrated that a simple $i - z$ cut can be an effective means of selecting $z > 5.5$ galaxies (Stanway et al. 2003; Bouwens et al. 2003b; B04; Dickinson et al. 2004). Since the surface densities of all known interlopers are expected to increase less quickly than bona-fide i -dropouts, we adopt the 11% found for brighter i -dropouts from GOODS (B04) as an upper limit to the contamination rate, with no spurious detections (running through a similar selection procedure on the negative images, no i -dropouts were found.) Given the similar incompleteness expected due to blending with foreground objects (verified through simulations, see B04), no net adjustment is made to the surface density.

(a) *Surface Density.* With the above selection criteria, we recovered 30 i -dropouts to a limiting $z_{850,AB}$ magnitude of 28.1, 20 in the first parallel and 10 in the second, suggesting a significant degree of clustering, but not inconsistent with the cosmic variance (50% RMS) expected for fields of this size (Somerville et al. 2004; B04). The luminosities of i -dropouts in our sample range from $1.1 L_*$ ($z_{850,AB} = 25.9$) to $0.15 L_*$ ($z_{850,AB} = 28.1$) (using the Steidel et al. (1999) value for L_* at $z \sim 3$). Half-light radii (uncorrected for PSF effects) range from 0.1'' to 0.3'', or 0.6 kpc to 1.7 kpc for the adopted set of cosmological parameters. The positions, magnitudes, sizes, $i - z$ colors, and SExtractor stellarity parameters of these objects are tabulated in Table 1.

(b) *Size Evolution.* Cosmic surface brightness dimming results in significant incompleteness at $z \sim 6$ (Bouwens et al. 2003b; Giavalisco et al. 2004; B04). To treat this, it is necessary to have a good estimate of the size (surface brightness) distribution (independent of selection effects). An empirical way of estimating this distribution is to model the observed sizes in terms of a scaled version of a lower redshift population and therefore derive the size evolution. For our low redshift comparison sample, we adopt the $z \sim 2.5$ HDF-N + HDF-S U -dropout sample (B04). The large $\Delta \log(1+z)$ increases our sensitivity to size changes. To artificially redshift this sample to $z \sim 6$ -weighting by $1/V_{max}$ and accounting for pixel k -corrections, surface brightness dimming, and detailed image properties like the noise and the PSF (as well as our selection procedure given above)—we employ the now well-

established cloning machinery (Bouwens, Broadhurst, & Silk 1998a,b; Bouwens et al. 2003a,b; B04). Finally, this redshifted sample is compared with a sample of i -dropouts ($z_{850,AB} < 27.2$) extracted from the ACS images degraded to the PSF of our U -dropout images projected to $z \sim 6$ (0.14'' FWHM) with a S/N equivalent to 5 orbit V_{606} , 10 orbit i_{775} , and 15-orbit z_{850} observations (0.6'' deeper than GOODS: see sample #2 from Table 1 for the objects used here).

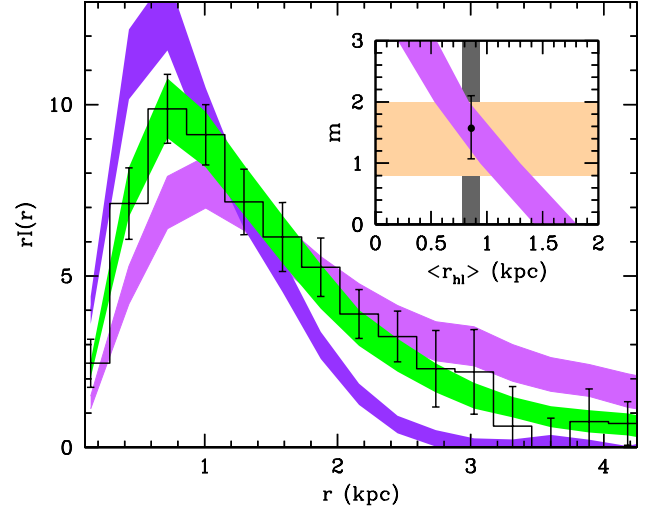


FIG. 1.— The mean radial flux profile for the 10 brightest $z_{850,AB} < 27.2$ i -dropouts (histogram, with $\pm 1\sigma$ uncertainties) in our sample versus the predictions based upon different scalings of the $z \sim 2.5$ HDF-N + HDF-S U -dropout sample (the i_{775} images available for this sample). The shaded violet, green, and dark violet regions represent predictions based upon the $(1+z)^0$, $(1+z)^{-1.5}$, and $(1+z)^{-3}$ size scalings, respectively. Clearly, the $(1+z)^{-1.5}$ scaling is a much better fit to the observations than the other two scalings. This is quantified in the figure inset, which shows the expected 1σ scatter (*diagonal violet band*) in the mean half-light radius vs. the $(1+z)^{-m}$ size scaling exponent m . Since the half-light radius for the mean profile is 0.85 ± 0.06 kpc (*plotted as a gray vertical band*), the inferred scaling is $(1+z)^{-1.57 \pm 0.53}$ (shown as the solid black circle with 1σ error bars) or $2.9^{+1.3}_{-0.8} \times$ from $z \sim 2.5$ to $z \sim 5.9$ (the mean redshifts of the U and i -dropout samples, B04). This is in good agreement with the allowed range of scalings ($m = 0.8 - 2.0$) inferred from a recent analysis of the GOODS data (B04) (*shaded in light orange*).

We consider size scalings of the form $(1+z)^{-m}$ ($m = 0 - 3$) (for fixed luminosity) and quantify the differences in terms of the mean radial flux profile, which provides a measure of the light within different circular annuli (see B04 for the computational details). The results of the procedure are shown in Figure 1 for the $(1+z)^0$, $(1+z)^{-1.5}$, and $(1+z)^{-3}$ scalings, and it is obvious that while the $(1+z)^{-1.5}$ scaling provides a good fit, the $(1+z)^0$ and $(1+z)^{-3}$ scalings produce profiles which are too broad and narrow, respectively (see Figure 2 for a visual comparison of the brighter dropouts with the no-evolution $m = 0$ scalings). To use these results to place confidence limits on the allowed scalings, we computed the mean size and variance for a 10-object sample of intermediate magnitude i -dropouts. The result is shown in the inset to Figure 1 as the shaded violet region. Given the observed half-light radius 0.85 ± 0.06 kpc (corrected for PSF effects) (*shaded grey region*), we infer an m of $1.57^{+0.53}_{-0.50}$ (*shown in the in-*

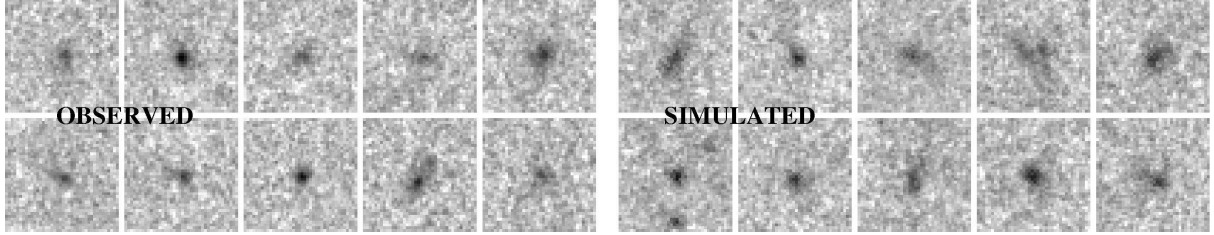


FIG. 2.— Postage stamp images (z_{850} -band) of 10 randomly-selected i -dropouts from the UDF-Ps ($z_{850,AB} < 27.2$) versus similarly selected no-evolution projections of our lower redshift HDF U -dropout sample (B04). The observed i -dropouts are both smaller and of higher surface brightness than the cloned U -dropout sample (a $2.9_{-0.8}^{+1.3} \times$ evolution in size, see Figure 1).

set as the solid circle with error bars), similar to what was found from our GOODS study (light orange region) where m was found to be between 0.8 and 2.0 (B04).

(c) *Luminosity/Density Evolution.* To interpret the i -dropout counts and therefore estimate the evolution of the LF, we use different projections of the lower redshift B -dropout sample from the GOODS fields (B04). We explore scalings in both luminosity (e.g., $(1+z)^l$) and number (e.g., $(1+z)^n$), assessing these scalings by comparing against both the UDF-Ps (degraded to the B -dropout PSF projected to $z \sim 6$, $0.1''$ FWHM with a S/N equivalent to 5 orbit V_{606} , 10 orbit i_{775} , and 15 orbit z_{850} observations; see sample #3 from Table 1 for the objects used here) and the GOODS fields (B04) (corrected up to the same completeness level as that of the UDF-Ps), which provide important constraints at bright magnitudes. As per the results of the previous subsection, sizes of individual B -dropouts are scaled as $(1+z)^{-1.5}$ (increasing their surface brightness). Interpolating between the simulation results and calculating a reduced χ^2 for each comparison, the 68% and 95% likelihood contours can be determined, taking as inputs the GOODS i -dropouts alone (shown in the Figure 3 inset as the green contours) and GOODS combined with the UDF-Ps (black contours). While the results from the UDF-Ps are helpful in breaking the degeneracy between luminosity and density evolution, small differences in normalization between the bright (from GOODS) and faint (from the UDF-Ps) counts could affect the results (due to cosmic variance). Deep wide-field images will be needed to ultimately establish the form of the evolution. The $(1+z)^{-2.8}$ scaling in number and $(1+z)^{0.1}$ scaling in luminosity preferred in this analysis point towards a $z \sim 6$ luminosity density ($\sim 1350 \text{ \AA}$) that is just $0.38_{-0.07}^{+0.09} \times$ that at $z \sim 3.8$ (error bars computed from 2D likelihood contours). Applying this factor to the $z \sim 3.8$ rest-frame continuum UV luminosity density determined by B04 and using standard assumptions to convert this into a star formation rate density (e.g., Madau, Pozzetti, & Dickinson 1998), the star formation history integrated down to $0.2 L_*$ can be plotted and compared with several previous determinations (Figure 4). The present result is noticeably lower. This is almost entirely the effect of size (surface brightness) evolution (see Figure 1) on the estimated completeness of the $z \sim 6$ census (and not due to our greater depth). Without size evolution from $z \sim 3.8$, the completeness correction and inferred luminosity density are some $\sim 1.9 \times$ higher than the current result (closer to previously published estimates: Bouwens et al. 2003b; Giavalisco et al. 2004; B04—see Figure 4).

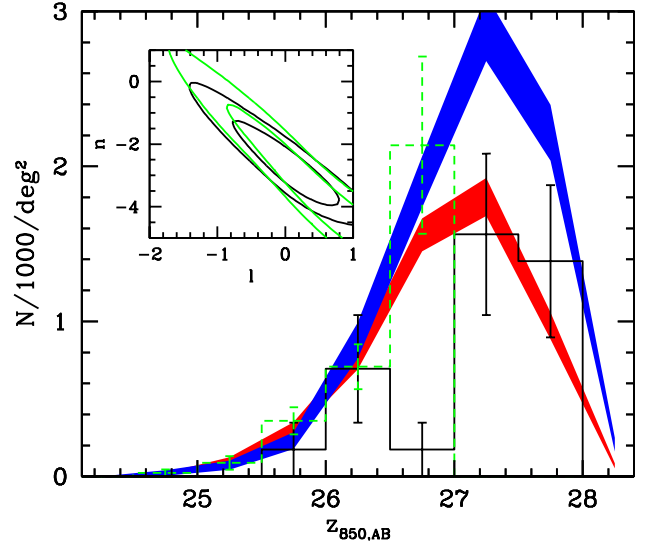


FIG. 3.— The observed number of i -dropouts per half magnitude interval observed in the UDF-Ps (solid black histogram shows the counts from the data degraded to match the projected PSF of the lower redshift samples [the undegraded data have an additional 8 objects beyond 27.5, see Table 1]) versus that predicted by a luminosity (blue-shaded region) and density (red-shaded region) scaling of the lower redshift B -dropout population. Each was scaled in size by $(1+z)^{-1.5}$ to match the evolution found in Figure 1 (the size scaling increased the B -dropout count predictions by 30-100%). The green histogram shows the number of i -dropouts per half magnitude interval observed in the GOODS fields using similar selection criteria (B04) corrected up to the completeness level of the UDF-Ps. The figure inset shows the 68% and 95% confidence intervals for luminosity evolution (parametrized as $(1+z)^l$) and density evolution (parametrized as $(1+z)^n$) taking as inputs the GOODS data alone (green contours) and the GOODS plus UDF parallel data (black contours). While the observations (bright i -dropouts from GOODS and faint i -dropouts from the UDF-Ps) prefer a model where $l = 0.1$ and $n = -2.8$, pure luminosity evolution or pure density evolution cannot be excluded (at 95% confidence).

(d) *Luminosity Function.* It is also useful to construct a simple estimate of the LF to examine the shape and look for evolution in the faint end slope. For our procedure, we follow Bouwens et al. (2003b) and treat the determination of the luminosity function $\phi(M)$ as a deconvolution problem on the integral $\int \phi(M(m, z))p(m, z) \frac{dV}{dz} dz = N(m)$ where $p(m, z)$ is the selection efficiency (including various factors ranging from galaxy color to photometric scatter to detectability), $N(m)$ is the number counts, and the absolute magnitude M here is given as a function of the apparent magnitude m and the redshift z (using an average color dropout to perform the k -correction). Adopting $N(m)$ from the primary data sets and taking $p(m, z)$ from the B -dropout cloning simulations (scaled in size as

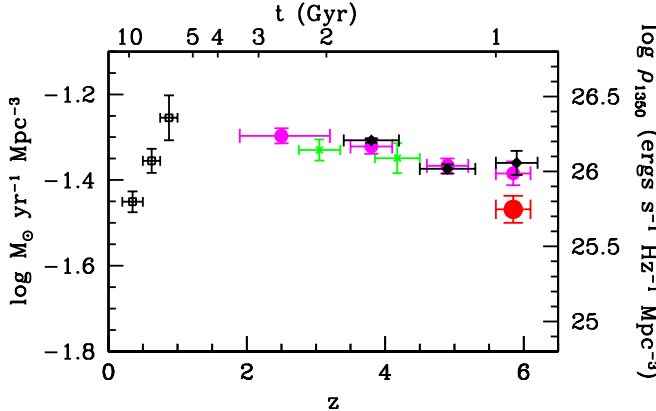


FIG. 4.— A history of the star formation rate density assuming no extinction correction, integrated down to $0.2L_*$. The red point at $z \sim 5.9$ represents our estimate based upon the i -dropouts found in both GOODS and the UDF-Ps (§3(c)). A Salpeter IMF is used to convert the luminosity density into a star formation rate (e.g., Madau et al. 1998). Comparison is made with the previous high redshift determinations of Lilly et al. (1996) (open squares), Steidel et al. (1999) (green crosses), Giavalisco et al. (2004) (solid black diamonds), and B04 (solid magenta circles). The top horizontal axis provides the corresponding age of the universe. The uncertainties for all determinations are formal errors. The inclusion of size evolution makes the present estimates lower than previous $z \sim 6$ estimates.

$(1+z)^{-1.5}$) (uncertain on the 20% level due to uncertainties in the size distribution), we are able to compute the LF and provide a simple fit to the Schechter function (Figure 5). Note that the relative normalization of the bright end of the LF ($M_{1350,AB} < -19.7$), determined primarily from GOODS, and the faint end of the LF, derived from the UDF-Ps, could vary by 36% RMS (the expected cosmic variance for a CDM-type power spectrum normalized to the high redshift observations, see B04), affecting the shape of the LF.

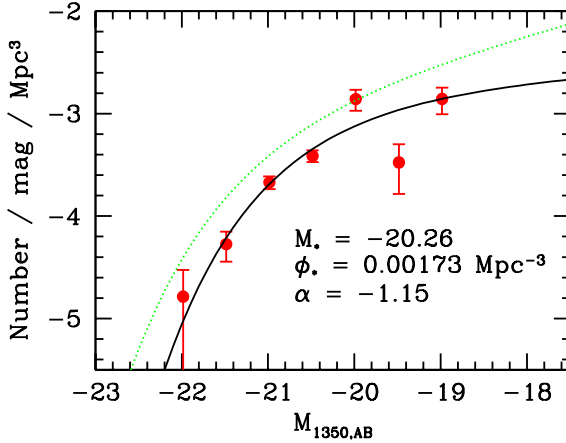


FIG. 5.— The rest-frame continuum UV ($\sim 1350\text{\AA}$) LF at $z \sim 6$ determined from the GOODS fields (at $M_{1350,AB} < -19.7$) and the UDF-Ps (red circles with 1σ error bars), with the best-fit LF to a Schechter function also shown ($M_{1350,AB,*} = -20.26$, $\phi_* = 0.00173 \text{ Mpc}^{-3}$, and $\alpha = -1.15$). The Steidel et al. (1999) $z \sim 3$ LF (dotted green line) is presented for comparison. A fit with $\alpha = -1.6$ (as observed at $z \sim 3$, Steidel et al. 1999) is also consistent (at 68% confidence) with the data, and yields values for $M_{1350,AB,*}$ ($= -20.77$) and ϕ_* ($= 0.00098 \text{ Mpc}^{-3}$) more suggestive of the interpretation given in §3(c) (an evolution in density).

4. DISCUSSION

The additional 0.9^m we have in z_{850} depth (and 1.1^m in $i775$) over the GOODS field allows us to probe further down the LF and obtain a wider distribution of sizes at bright magnitudes than was possible from previous data. This depth largely compensates for the $(1+z)^4$ cosmic surface brightness dimming, allowing us to set a more direct constraint on object sizes at $z \sim 6$ (cf. B04). The results here are consistent with the $(1+z)^{-1.5}$ scaling of size found at lower redshift ($1 < z < 5$) for objects of fixed luminosity (Ferguson et al. 2004), extending the trend to $z \sim 6$. This evolution in size has important implications for the luminosity density inferred at this epoch, suggesting that the star formation rate density has increased significantly from $z \sim 6$.

In this work, we present the first robust luminosity function at $z \sim 6$ and find no radical difference relative to lower redshift. While the UDF will add depth and further constraints, the present fields provide a crucial assessment of the cosmic variance.

We would like to thank Narciso Benítez, Emmanuel Bertin, Fred Courbin, Michele de la Pena, Harry Ferguson, Andy Fruchter, Dave Golimowski, Dan Magee, and Jon McCann for their assistance and the referee for valuable comments. We acknowledge the support of NASA grant NAG5-7697 and NASA grant HST-GO9803.05-A.

REFERENCES

- Bennett, C. L. et al. 2003, ApJ, 583, 1.
- Bertin, E. and Arnouts, S. 1996, A&AS, 117, 393.
- Blakeslee, J. P., Anderson, K. R., Meurer, G. R., Benítez, N., & Magee, D. 2003a, ASP Conf. Ser. 295: Astronomical Data Analysis Software and Systems XII, 12, 257.
- Bouwens, R., Broadhurst, T. and Silk, J. 1998a, ApJ, 506, 557.
- Bouwens, R., Broadhurst, T. and Silk, J. 1998b, ApJ, 506, 579.
- Bouwens, R., Broadhurst, T., & Illingworth, G. 2003a, ApJ, 593, 640.
- Bouwens, R. J. et al. 2003b, ApJ, 595, 589.
- Bouwens, R.J., Broadhurst, T.J., Illingworth, G.D., Meurer, G.R., Blakeslee, J.P., Franx, M., & Ford, H.C. 2004, ApJ, submitted (B04).
- Dickinson, M. et al. 2004, ApJ, 600, L99.
- Ferguson, H. C. et al. 2004, ApJ, 600, L107
- Giavalisco, M. et al. 2004, ApJ, 600, L103
- Lilly, S.J., Le Fevre, O., Hammer, F., & Crampton, D. 1996, ApJ, 460, L1.
- Madau, P., Pozzetti, L. & Dickinson, M. 1998, ApJ, 498, 106.
- Schlegel, D. J., Finkbeiner, D. P., & Davis, M. 1998, ApJ, 500, 525.
- Sirianni, M., et al. 2004, in preparation.
- Somerville, R. S., Lee, K., Ferguson, H. C., Gardner, J. P., Moustakas, L. A., & Giavalisco, M. 2004, ApJ, 600, L171.
- Stanway, E. R., Bunker, A. J., & McMahon, R. G. 2003, MNRAS, 342, 439.
- Stanway, E. R., Bunker, A. J., & McMahon, R. G., Ellis, R., Treu, T., & McCarthy, P. 2004, ApJ, in press.
- Steidel, C. C., Adelberger, K. L., Giavalisco, M., Dickinson, M. and Pettini, M. 1999, ApJ, 519, 1.
- Thompson, R. I., et al. 2004, in preparation.
- Yan, H., Windhorst, R. A., & Cohen, S. H. 2003, ApJ, 585, L93.

TABLE 1
 $z \sim 6$ OBJECTS FROM THE UDF-Ps.^a

Object ID	Right Ascension	Declination	z_{850}	$i - z$	S/G	$r_{hl}(\text{''})$	Sample
UDFP1-4109-2788	03:32:42.692	-27:56:55.35	25.9 \pm 0.1	1.8	0.00	0.34	3
UDFP1-3629-862	03:32:49.638	-27:56:27.47	26.2 \pm 0.2	2.0	0.02	0.26	3
UDFP1-3851-2438	03:32:43.958	-27:56:43.86	26.3 \pm 0.1	1.6	0.18	0.11	1,2,3
UDFP1-4650-3354	03:32:40.706	-27:57:24.28	26.4 \pm 0.1	1.7	0.02	0.18	1,2,3
UDFP1-1546-1408	03:32:47.047	-27:54:48.09	26.9 \pm 0.1	1.4	0.00	0.19	2
UDFP1-2954-1152	03:32:48.367	-27:55:54.81	26.9 \pm 0.2	1.5	0.37	0.11	2
UDFP1-4040-2514	03:32:43.709	-27:56:50.93	27.0 \pm 0.2	1.9	0.01	0.19	1,2,3
UDFP1-2309-1628	03:32:46.409	-27:55:24.31	27.1 \pm 0.1	>2.5	0.02	0.11	1,2,3
UDFP1-4784-3382	03:32:40.634	-27:57:31.07	27.2 \pm 0.2	1.6	0.02	0.14	1,2,3
UDFP1-3350-3425	03:32:40.111	-27:56:22.32	27.4 \pm 0.2	1.5	0.01	0.12	1,2,3
UDFP1-4413-3612	03:32:39.671	-27:57:13.38	27.4 \pm 0.2	>2.1	0.02	0.11	1,2,3
UDFP1-3144-2410	03:32:43.876	-27:56:08.48	27.4 \pm 0.2	>1.8	0.01	0.19	1
UDFP1-1188-2375	03:32:43.512	-27:54:33.43	27.5 \pm 0.2	>2.2	0.01	0.10	1,2,3
UDFP1-3162-3232	03:32:40.791	-27:56:12.25	27.5 \pm 0.2	>1.8	0.00	0.15	1
UDFP1-3407-1028	03:32:48.952	-27:56:16.97	27.5 \pm 0.2	1.7	0.02	0.10	1,2,3
UDFP1-886-1917	03:32:44.962	-27:54:16.93	27.6 \pm 0.2	>1.9	0.01	0.12	1,3
UDFP1-2347-2492	03:32:43.360	-27:55:29.04	27.6 \pm 0.2	1.5	0.02	0.11	1,2
UDFP1-3515-1622	03:32:46.745	-27:56:24.45	27.7 \pm 0.2	>1.8	0.00	0.14	1
UDFP1-3958-2376	03:32:44.206	-27:56:46.38	27.7 \pm 0.1	2.3	0.07	0.07	1,2,3
UDFP1-1669-3099	03:32:40.914	-27:54:59.91	27.8 \pm 0.2	1.4	0.01	0.11	1,3
UDFP1-2766-1640	03:32:46.480	-27:55:47.12	27.8 \pm 0.2	1.7	0.01	0.11	1,3
UDFP1-4522-2133	03:32:45.269	-27:57:13.66	27.9 \pm 0.2	>1.8	0.24	0.09	1,3
UDFP1-1075-2025	03:32:44.801	-27:54:26.57	28.0 \pm 0.2	1.5	0.01	0.10	1
UDFP1-2284-2177	03:32:44.529	-27:55:24.81	28.1 \pm 0.2	>1.6	0.01	0.11	1
UDFP2-1391-2218	03:32:06.504	-27:48:46.86	26.3 \pm 0.1	1.6	0.02	0.21	1,2,3
UDFP2-3139-2714	03:32:00.000	-27:48:27.90	27.0 \pm 0.2	1.6	0.09	0.19	3
UDFP2-1740-2767	03:32:05.051	-27:48:20.66	27.2 \pm 0.2	1.6	0.00	0.19	1,3
UDFP2-1371-4301	03:32:06.056	-27:47:05.48	27.2 \pm 0.2	1.6	0.02	0.11	1,2,3
UDFP2-3571-2314	03:31:58.476	-27:48:49.34	27.5 \pm 0.2	1.4	0.19	0.13	2
UDFP2-3846-4219	03:31:56.968	-27:47:17.85	27.6 \pm 0.2	>1.9	0.01	0.13	1
UDFP2-2451-4421	03:32:02.159	-27:47:03.04	27.6 \pm 0.2	1.5	0.01	0.12	3
UDFP2-2600-3957	03:32:01.721	-27:47:26.64	27.7 \pm 0.2	>1.6	0.00	0.17	1
UDFP2-3047-2428	03:32:00.420	-27:48:41.89	27.7 \pm 0.2	>1.6	0.00	0.12	3
UDFP2-1637-2294	03:32:05.560	-27:48:43.92	27.9 \pm 0.2	1.5	0.03	0.09	1
UDFP2-2704-2415	03:32:01.712	-27:48:41.35	28.0 \pm 0.2	1.8	0.01	0.09	1,3
UDFP2-1185-3335	03:32:06.990	-27:47:50.46	28.0 \pm 0.2	1.7	0.01	0.09	1
UDFP2-2634-3361	03:32:01.733	-27:47:53.91	28.0 \pm 0.2	>1.6	0.01	0.12	1
UDFP2-1897-3880	03:32:04.175	-27:47:25.68	28.1 \pm 0.2	1.4	0.01	0.09	1

^aSelection criteria: $(i_{775} - z_{850})_{AB} > 1.4$ plus null detection ($< 2\sigma$) in V_{606} . All limits are 2σ . “S/G” denotes the SExtractor stellarity parameter, for which 0 = extended object and 1 = point source. Several different samples were used in the analysis. Sample #1 was generated by applying our selection criteria to the undegraded images. Sample #2 and #3 were generated by applying these selection criteria to the images degraded to match the PSF of the U and B -dropout samples, respectively, projected to $z \sim 6$ ($0.14''$ FWHM and $0.10''$ FWHM). Images from the latter samples were degraded to a uniform S/N equivalent to 5 orbit V_{606} , 10 orbit i_{775} , and 15 orbit z_{850} observations. The union of all three samples (38 objects) is larger than the undegraded sample (sample #1) due to object blending and photometric scatter. UDFP1 and UDFP2 refer to the first and second UDF parallels, respectively.